Performance Evaluation of a Smart Mobile Air Temperature and Humidity Sensor for Characterizing Intracity Thermal Environment

CHANG CAO,[a,b] YICHEN YANG,[c] YANG LU,[a,b] NATALIE SCHULTZE,[c] PINGYUE GU,[d] QI ZHOU,[d] JIAPING XU,[e] AND XUHUI LEE[c]

[a] *Yale–NUIST Center on Atmospheric Environment, Nanjing University of Information Science and Technology, Nanjing, Jiangsu, China;* [b] *Jiangsu Key Laboratory of Agriculture Meteorology, Nanjing University of Information Science and Technology, Nanjing, Jiangsu, China;* [c] *School of the Environment, Yale University, New Haven, Connecticut;* [d] *Jiangsu Radio Scientific Institute, Co., Ltd., Wuxi, China;* [e] *Jiangsu Climate Center Nanjing, China*

(Manuscript received 4 February 2020, in final form 13 August 2020)

ABSTRACT: Heat stress caused by high air temperature and high humidity is a serious health concern for urban residents. Mobile measurement of these two parameters can complement weather station observations because of its ability to capture data at fine spatial scales and in places where people live and work. In this paper, we describe a smart temperature and humidity sensor (Smart-T) for use on bicycles to characterize intracity variations in human thermal conditions. The sensor has several key characteristics of internet of things (IoT) technology, including lightweight, low cost, low power consumption, ability to communicate and geolocate the data (via the cyclist's smartphone), and the potential to be deployed in large quantities. The sensor has a reproducibility of 0.03°–0.05°C for temperature and of 0.18%–0.33% for relative humidity (one standard deviation of variation among multiple units). The time constant with a complete radiation shelter and moving at a normal cycling speed is 9.7 and 18.5 s for temperature and humidity, respectively, corresponding to a spatial resolution of 40 and 70 m. Measurements were made with the sensor on street transects in Nanjing, China. Results show that increasing vegetation fraction causes reduction in both air temperature and absolute humidity and that increasing impervious surface fraction has the opposite effect.

KEYWORDS: Instrumentation/sensors; Urban meteorology

1. Introduction

Heat stress caused by high temperature and high humidity is among the most serious climate threats to society (Revi et al. 2014). The problem is further exacerbated for urban residents due to the urban heat island (UHI), the phenomenon of higher temperatures in cities than in the adjacent rural lands (Oke et al. 2017). A large body of literature has been devoted to characterizing of the UHI strength and to understanding drivers of its geographic, seasonal, and diurnal variations (e.g., Arnfield 2003; Voogt and Oke 2003; Mirzaei and Haghighat 2010; Zhou et al. 2019). Traditionally, a city is considered as a single unit having one UHI value. In recent years, an increasing number of studies have investigated intracity temperature variations. Central to these studies is this question: How do urban morphological attributes influence the release, dispersion, diffusion and trapping of energy? This question is important for assessing urban environmental vulnerability because urban morphology (green space, impervious surface fraction, and building density) may be linked to socioeconomic status of urban neighborhoods and to spatial patterns of demographic and ethnic compositions (Chakraborty et al. 2019). A good understanding of association between urban morphology and spatial distribution of temperature can inform neighborhood-scale heat mitigation strategies (Bowler et al. 2010; Gunawardena et al. 2017; Ziter et al. 2019).

Although it is well established that lower temperatures are associated with green spaces and higher temperatures with buildup areas of a city, we lack consistent and quantitative information regarding the spatial extent of influence or source footprint of these land features on urban air temperature. Such information is essential for planning of green infrastructure for heat mitigation (Gunawardena et al. 2017). In geospatial modeling of the urban thermal environment, source footprint size is needed for spatial aggregation to increase the predicting power of the model (Schatz and Kucharik 2014; Heusinkveld et al. 2014; Venter et al. 2020). Theoretical footprint models suggest that the source footprint of an urban weather station is about 500 m in radius (Oke 2006). However, these models are established on the condition that air turbulence near the ground should be horizontally homogeneous (Horst 2001; Schmid 2002), a condition that strictly does not hold in cities where the landscape is always heterogeneous. Alternatively, the source footprint can be determined empirically by examining the spatial correlation between measured temperature and green or impervious surface fraction in varying buffer sizes (Heusinkveld et al. 2014). The few published estimates of urban temperature footprint vary by an order of magnitude, from about 70 m for Madison, Wisconsin (Ziter et al. 2019), to 1600 m for Rotterdam, the Netherlands (Heusinkveld et al. 2014). More observational studies are needed to understand how the source footprint vary diurnally, seasonally and between different background climates.

Supplemental information related to this paper is available at the Journals Online website: https://doi.org/10.1175/JTECH-D-20-0012.s1.

Corresponding author: Xuhui Lee, xuhui.lee@yale.edu

DOI: 10.1175/JTECH-D-20-0012.1

Another less understood aspect of the urban thermal environment is intracity variations in air humidity. Humidity is an important variable for human health consideration because high air humidity increases the severity of heat stress in a heatwave event. According to observations in London, United Kingdom (Lee 1991), Goteborg, Sweden (Holmer and Eliasson 1999), Munich, Germany (Mayer et al. 2003), and Krefeld, Germany (Kuttler et al. 2007), the urban–rural differences in humidity and in air temperature are positively correlated over time. Whether this temporal correlation can be extended to describe intracity spatial variations in humidity is not known. So far, simultaneous observations of these two variables across space have been rather limited, and the results remain inconclusive. Mobile measurements made in street transects of Gaborone, Botswana (Jonsson 2004), suggest that temperature and humidity may be negatively correlated over space, meaning that cooler neighborhoods may be associated with more humid air. Observations made with a network of fixed stations in Matsuyama, Japan, seem to show a negative spatial correlation at night and a positive correlation in the day (Chhetri et al. 2017). Although a predictive understanding exists for intracity spatial patterns of air temperature (Brandsma and Wolters 2012; Heusinkveld et al. 2014; Schatz and Kucharik 2014), little is known about how land surface features themselves and their interactions with air temperature influence intracity variabilities in humidity. Simultaneous observations of temperature and humidity should provide more accurate assessment of heat mitigation strategies than measurement of temperature alone. For example, if a patch of green vegetation reduces temperature but increases humidity, the net cooling benefit of the vegetation would be smaller than that solely based on temperature reduction.

Although high-resolution (tens of meters) land-use data are available for cities from satellite monitoring (Gong et al. 2020; Li et al. 2020), high-resolution observations of air temperature and humidity remain scanty. Using crowdsourced temperature data in Oslo, Norway, Venter et al. (2020) showed that a station density better than 1 km^{-2} is needed to accurately map urban temperature. Mesoscale networks of surface weather station in urban airsheds have a spatial resolution ranging from about 10 to 2 km (Grimmond 2006; Koskinen et al. 2011; Basara et al. 2011; Hung and Wo 2012; Muller et al. 2013; Chapman et al. 2015; Warren et al. 2016; Chen et al. 2018; Wang et al. 2018; Li et al. 2018). Crowdsourcing from personal weather stations (Muller et al. 2015; Meier et al. 2017; Hammerberg et al. 2018) and smartphones (Overeem et al. 2013; Droste et al. 2017) can improve the spatial resolution up to 0.1 km^2 (Venter et al. 2020). So far, crowdsourcing studies have focused on temperature, and we are not aware of a similar investigation of both air temperature and humidity.

Mobile sensors are suited for neighborhood-scale measurements of temperature and humidity in a city. This approach is versatile and is especially useful for urban areas that do not have weather stations or have sparsely placed weather stations (Hedquist and Brazel 2006). Although they underperform in detecting daily maximum temperature in comparison to stationary monitoring (Yang and Bou-Zeid 2019), they allow continuous measurement along land-use transitions. Mobile measurement is commonly done with sensors carried by automobiles (e.g., Unger et al. 2001; Qaid et al. 2016; Leconte et al. 2017; Shi et al. 2018). Several studies have deployed sensors carried by pedestrians (Tsin et al. 2016; Pigliautile and Pisello 2018; Runkle et al. 2019). Automobiles can travel long transects in a short time, while pedestrians cannot. Because the car travels at a relatively high speed (more than 30 km h^{-1}), fast-responding sensors are needed to capture temperature and humidity variations along the road traveled. Bicycles can also serve as mobile measurement platforms. Bicycles can travel to places that may not be accessible by cars. They do not generate heat or moisture and therefore will not interfere with the monitoring. Moving at reasonable speeds (3–5 m s^{-1}), they can cover long street transects (e.g., 10 km) within a short time window of 30–60 min. For sensors with a response time of 10 s, these travel speeds correspond to spatial resolutions of 30–50 m, which are fine enough for capturing neighborhood-scale microclimatic variations. In the past, several research groups have used bicycle-mounted sensors to measure air temperature along street transects (Brandsma and Wolters 2012; Yan et al. 2014; Rajkovich and Larsen 2016; Yan et al. 2018; Yokoyama et al. 2018; Ziter et al. 2019).

The apparatus used in most of the mobile studies cited above are basically bulky weather stations consisting of a sensor, a datalogger, a battery pack and a GPS unit. They are not practical for large-scale deployment due to their size and cost. Furthermore, to our best knowledge, except for Jonsson (2004) and Noro et al. (2015), the published mobile studies either have limited their observation to temperature or have observed both temperature and humidity but have only reported the temperature data.

In this study, we describe a smart sensor that satisfies the four essential functions required for mobile measurement: sensing of temperature and humidity, datalogging, time stamping, and geolocating. The sensor has the characteristics of the internet of things (IoT) technology: it is lightweight and low cost, has wireless data communication ability, and can be potentially deployed in large quantities. Our objectives are 1) to characterize the performance of this sensor in terms of accuracy, reproducibility, and time response; 2) to investigate spatial variabilities of air temperature and humidity and their source footprints in an urban sector; and 3) to analyze the interactions between temperature, humidity, and surface morphology.

2. Materials and methods

a. Sensor description

The sensor unit, called Smart-T, is 85 mm tall (Fig. 1a). The outer body, made of white acrylonitrile butadine styrene, is a radiation shield with ventilation openings at the top. Housed in the shield is a small (4.2 cm × 2.5 cm) circuit board that integrates the sensor electronics and a Bluetooth module. The sensing element is isolated at 1.1 cm away from the main circuit to enhance its time response, and is positioned in the middle of the ventilation openings to maximize the exchange with ambient air when the bicycle is in motion. The whole unit is powered by a button battery (20 mm diameter,

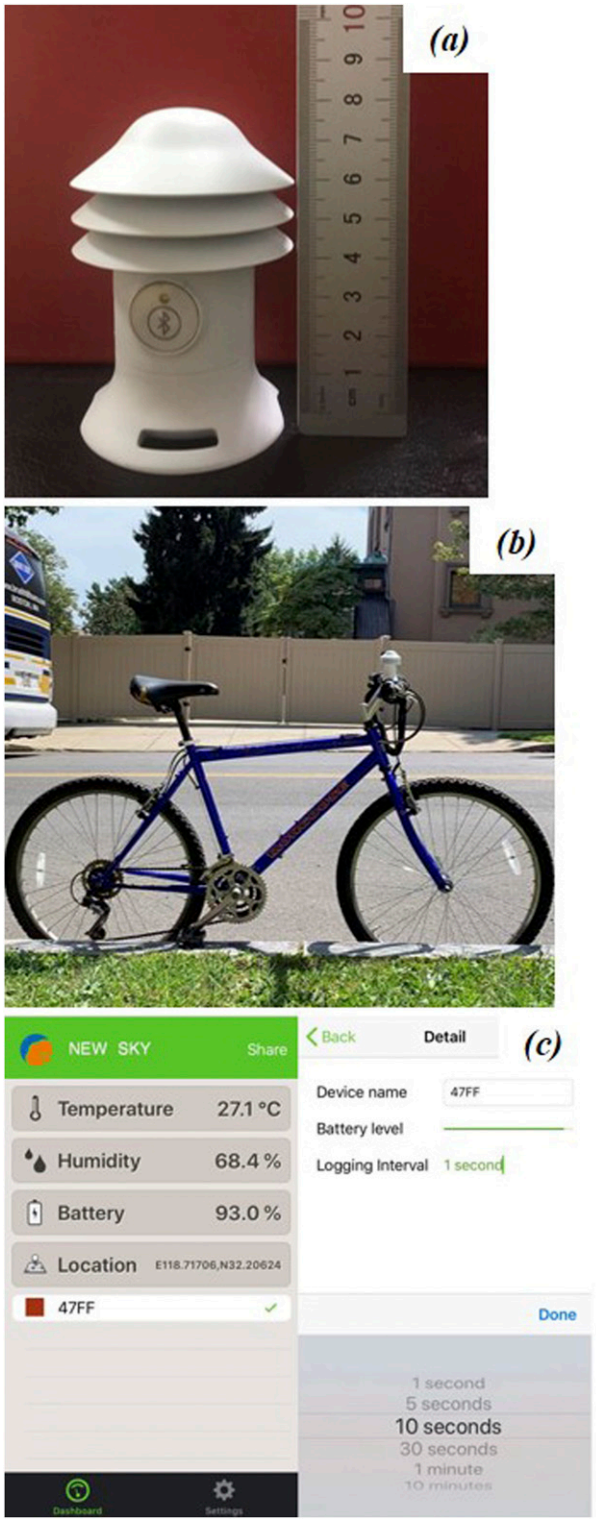

FIG. 1. (a) Photographs of a Smart-T unit and (b) a Smart-T unit mounted on a bicycle, as well as (c) the smartphone app interface and data display for the IOS system.

Panasonic CR2032) with negligible heat production. A typical battery life is 6 months. In the field operation, the sensor is fastened on the crossbar of a bicycle (Fig. 1b). The sensing element can measure air temperature in the range from −40° to 60°C with a 0.01°C resolution and relative humidity (RH) in the range from 10% to 90% with a 0.01% resolution.

A smartphone app, available for Android and IOS operating systems, converts the cyclist's mobile phone to a datalogging and positioning device (Fig. 1c). Each Smart-T unit has a unique Bluetooth tag. Once connected, the phone will display air temperature and RH readings and the battery condition. The user can select a sampling interval from 1 s to 10 min. The data are saved as .txt file on the Android system. For the IOS system, other data formats are also available. The data file has six columns: Bluetooth tag, time, latitude, longitude, air temperature, and RH.

b. *Tests in calibration chambers*

Two Smart-T units (tags 337D and F9A3) were tested in the temperature and humidity calibration chambers belonging to the Jiangsu Radio Scientific Institute Co., Ltd., Wuxi, China. The type of temperature chamber is SU-662 (ESPEC Corp., Osaka, Japan) with temperature range from −70° to 150°C and that of humidity chamber is C4-340 (Weiss-Voetsch, Taicang, China) with RH range from 10% to 98%. These facilities are certified by Shanghai Institute of Measurement and Testing Technology and National Institute of Metrology in China for calibrating operational temperature and humidity sensors for WMO baseline weather stations in China. For comparison, a commercial mobile temperature–humidity sensor for use with unmanned aerial vehicles (model I-Met XQ2, InterMet Systems Inc., Grand Rapids, Michigan) was also tested. In the first test (of temperature measurement), the calibration chamber was stepped through four air temperature targets (50°, 30°, 0°, −20°C), each lasting 20–30 min. The temperature measured by a WUSH-TW100A sensor (Jiangsu Radio Scientific Institute Co., Ltd.) served as the true value in this test. RH in the temperature chamber was not recorded during the test, but it usually does not exceed 40% for low temperatures and it will not drop below 20% for high temperatures. In the second test (of humidity measurement), the chamber was stepped through five RH levels (30%, 50%, 70%, 90%, and 95%), each lasting 20–30 min. Temperature during the second test was about 20°C. The humidity measured by a DHC2 probe (Jiangsu Radio Scientific Institute Co., Ltd.) served as the calibration standard for this test. These standard temperature and humidity instruments are calibrated annually by the Measurement and Testing Institute of China.

c. *Characterization of reproducibility among multiple sensors*

Two indoor experiments were conducted to characterize the reproducibility, using a total of 39 Smart-T sensors. One experiment took place in the Yale Center for Earth Observation (YCEO) Laboratory, in New Haven, Connecticut, and the other in the Yale–Nanjing University of Information Science and Technology (NUIST) Center on Atmospheric Environment (YNCenter) Laboratory, in Nanjing, China. The experimental

rooms were sealed. In the YCEO experiment, 30 Smart-T sensors were placed in close proximity on a table, along with three HOBO temperature and humidity sensors (Model MX2302A, Onset Computer Corporation, Bourne, Massachusetts). Two fans at the two ends of the table blew air toward each other, mixing the air uniformly across the sensors. A smartphone scanned the Smart-T sensors sequentially, retrieving data for 5 min at 1 s intervals from each, while the HOBO sensors recorded the data continuously. The experiment lasted 3 h, during which the temperature varied between 25.8° and 26.1°C and the humidity between 43.5% and 44.5%. Air temperature and RH deviations were computed by subtracting the mean values of the three HOBO sensors during the same 5 min period from the Smart-T value. Because the room temperature and humidity were not controlled precisely, using HOBO sensors as the reference removed the background variations. Reproducibility among the tested sensors is high if the deviations are similar among them.

The YNCenter experiment followed the same procedure as the YCEO experiment, with two modifications. The number of Smart-T sensors was 9 and the reference readings were provided by two I-Met XQ2 sensors. The experiment lasted 2 h. Temperature and humidity varied between 30.4° and 30.9°C and between 51% and 53% during this experiment.

d. Characterization of sensor time response

To characterize its time response, we subjected a Smart-T sensor (tag E659, in radiation shelter housing) to step changes in temperature and humidity. After the sensor had been brought to equilibrium with the room temperature and humidity, it was moved to the outside on a bicycle at a normal travel speed of 4 $m\,s^{-1}$. The temperature and humidity time series recorded during the transition from the indoor to the outdoor condition were used to determine the time constants of the temperature and the humidity measurements. This process was repeated four times.

e. Outdoor transects

We compared a Smart-T sensor (tag 6FD2) with an I-Met XQ2 (57540) sensor, both attached to the handle-bar of a bicycle, along a 4.8-km-long street transect on the campus of NUIST, in Nanjing, China. The whole route followed a zigzag pattern in a west to the east direction (Fig. 2). The two ends of the route were open streets with minimal tree cover and green vegetation, and the middle section of the route consisted of streets with large trees and tall buildings. At the time of the measurement [1430–1451 local time (LT) 8 November 2019], the sky was clear, with the incoming solar radiation flux of 317 $W\,m^{-2}$.

Repeated measurements of air temperature and humidity were made with a Smart-T sensor (tag 6FD2) from 21 to 24 July and from 30 July to 1 August 2019. The measurement route, also on the NUIST campus, consisted of several streets that formed a loop pattern and a linear transect, with a total length of 4 km (Figs. 3 and 4). The eastern section of the loop was a busy highway, and the rest of the route traversed the campus sports fields and zones with median-density residual and classroom buildings. The points on the loop were sampled once and the points on the linear transect were sampled twice (in forward and return trip) during each observation. Four observations were made in each day, starting at 0500, 1400, 1900 and 2200 LT. A total of 28 observations was made (7 days × 4 times a day). The sensor was brought to the outside 20 min before the start of each observation. Each observation lasted about 17 min. The sky during the 7 observational days was clear to partly cloudy. Air temperature varied between 25.6° and 38.8°C, and RH between 44% and 92%. The wind speed varied between 0.1 and 2.9 $m\,s^{-1}$.

We used the wet-bulb temperature (T_w) as an indicator of the combined effect of air temperature and humidity on human health. The wet-bulb temperature was solved numerically (Moratiel et al. 2017) from the wet-bulb equation (e.g., Lee 2018)

$$T_w + \frac{e_v^*(T_w)}{\gamma} = T_a + \frac{e_a}{\gamma}, \tag{1}$$

where T_a is the observed air temperature, γ is psychrometric constant, e_v^* is saturated vapor pressure, and e_a is the vapor pressure determined from the measured air temperature and RH.

We chose T_w instead of the empirical humidity index (Ho et al. 2014; Scott et al. 2017; Jiang et al. 2019) because the former is a thermodynamic variable that controls directly the heat exchange between the environment and the human body (Sherwood and Huber 2010). Other heat stress indices require simultaneous measurements of solar radiation or wind speed (e.g., Cohen et al. 2012), which were not available from our transect observations.

f. Land-cover classification

PlanetScope satellite imagery acquired on 27 July 2019 (3.8 m resolution with blue, green, red, and near-infrared bands) was used to produce land-cover classification. The classifier was a convolutional neural network scheme containing a feature called skip connection to enable pixel-wise prediction. It segmented the image into 6 classes, including tree, grass, bare soil, water, building, and impervious ground. The training set consisted of 390 pixels × 1160 pixels. The overall accuracy was 90%. Vegetation fraction and impervious surface fraction in each buffer area were based on the vegetation pixel (tree and grass) count and the impervious pixel (building and impervious ground) count, respectively.

3. Results

a. Characterization of sensor performance

1) Accuracy and time response

Figure 5 summarizes the chamber test results. The error in Smart-T air temperature measurements ranged from −0.01° to 0.48°C, with larger values when air temperature was below freezing than in warmer conditions (Fig. 5a). For comparison, the I-Met XQ2 sensor showed smaller temperature errors (0.07° to 0.36°C) than the Smart-T sensors. The error in Smart-T RH did not exceed 1.9% in magnitude and was smaller than the I-Met XQ2 error (up to 2.9% in magnitude; Fig. 5b).

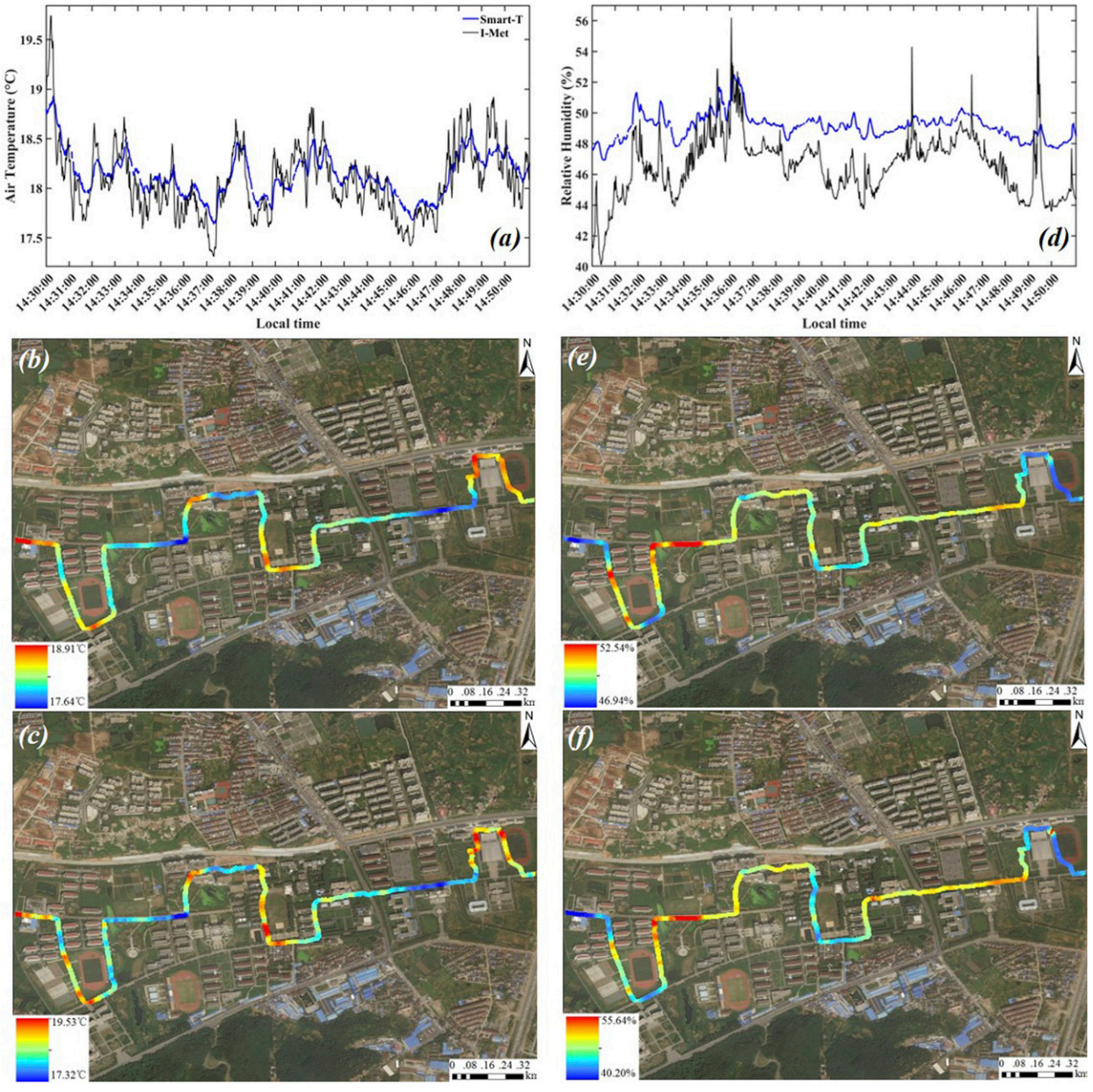

FIG. 2. (a),(d) Time series and (b),(c),(e),(f) spatial map of air temperature and relative humidity measured with (b),(e) a Smart-T (tag 6FD2) and (c),(f) a I-Met XQ2 (57540) sensor. The map background is a true-color satellite image.

The largest temperature error recorded in this test (0.48°C at temperature of −0.20°C) exceeded the manufacturer's specification for the Smart-T sensing element (±0.3°C). The measurement error became smaller at higher temperatures (0.19° and 0.23°C at 29.50°C and −0.01° and 0.15°C at 49.35°C; Fig. 5a).

Figure 6 is an example of the sensor response to step changes in air temperature and humidity. In this case, the time constant was 9.6 s for air temperature and 19.3 s for RH. The mean time constant (average of four step-change tests) was 9.7 (±3.2) s (mean ± one standard deviation) for air temperature and 18.5 (±4.3) s for RH. At a typical bicycle traveling speed of 4 m s^{-1}, the Smart-T measurement had a spatial resolution of about 40 m for air temperature and 70 m for humidity.

A comparison with the I-Met unit can be found in Fig. 2 from a street transect observation. The average air temperature from the Smart-T sensor was 18.13°C and that from the I-Met XQ2 sensor was 18.07°C, giving a difference of 0.06°C. The average RH from the Smart-T was 49.1%, which was 2.6% higher than that of the I-Met reading. Because of its fast time response (time constants are 2 s for air temperature and 5 s for humidity at a travel speed of 1 m s^{-1}), the I-Met measurement showed larger fluctuations than the Smart-T readings (Figs. 2a,d). The air temperature and RH differences between

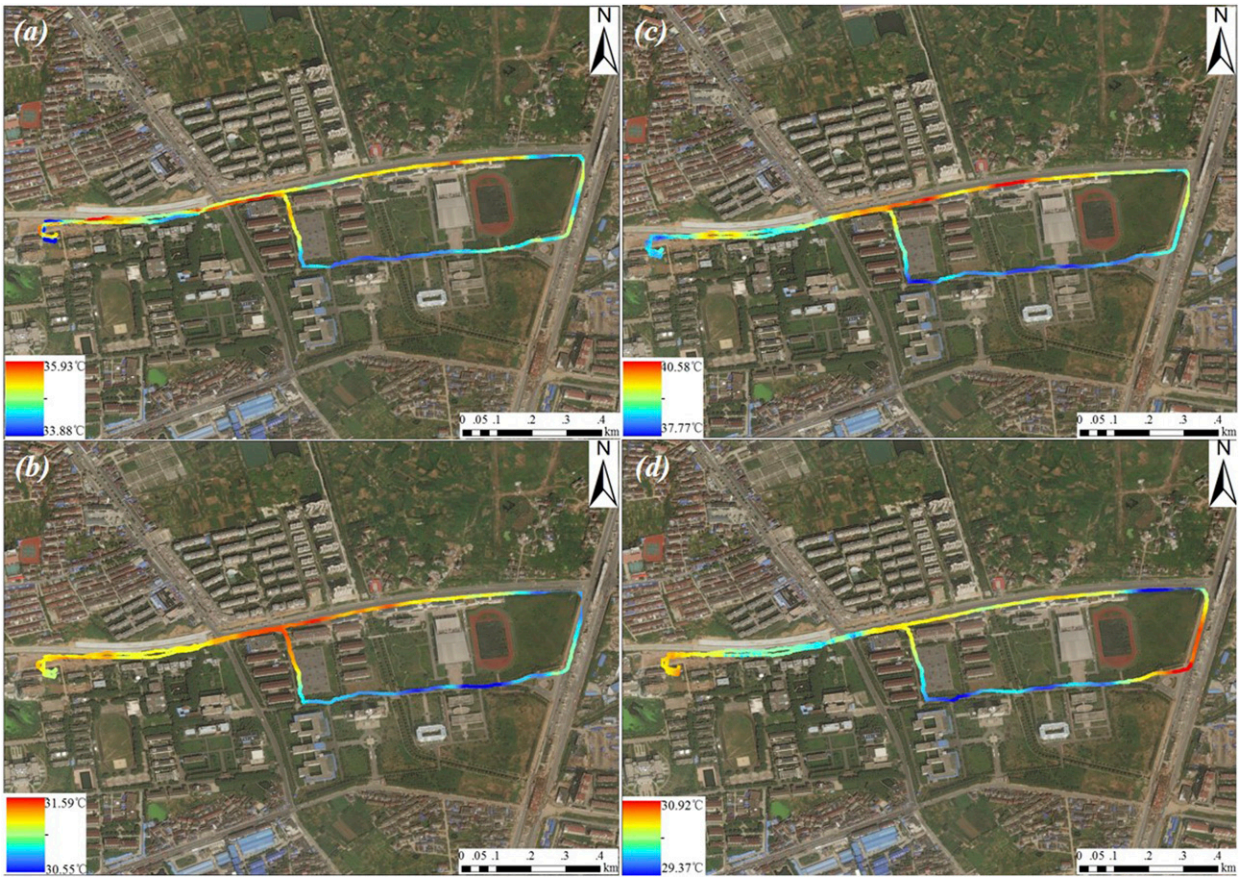

FIG. 3. Spatial variations in air temperature at (a) 1400 and (b) 2200 LT 24 Jul and (c) 1400 and (d) 2200 LT 31 Jul 2019. The map background is a true-color satellite image.

the two sensors were poorly correlated with vegetation cover fraction (Fig. S1 in the online supplemental material) and their spatial patterns did not seem to correspond to street orientation (Fig. S2). Eleven datapoints showed a negative RH difference (Smart-T minus I-Mets) smaller than −2%; these occurred in places having trees or near water bodies. Some of the fluctuations recorded by I-Met were unwanted because they were associated with random turbulent motion and were not related to the underlying land surface features. The overall spatial patterns showed quite good agreement between the two sensors in terms of air temperature (Figs. 2b,c) and RH (Figs. 2e,f).

2) REPRODUCIBILITY

In the YCEO indoor comparison experiment, the Smart-T sensors showed slightly lower air temperature reading than the HOBO sensors. Their difference (Smart T minus HOBO) ranged from −0.01° to −0.17°C with a median value −0.10°C (Fig. 7a). The RH recorded by Smart-T was generally higher than that of HOBO, and the offset was in the range from 2.75% to 3.68% with a median value of 3.40% (Fig. 7b). The Smart-T sensor has the potential to be deployed in large quantities in the future. Toward that end, high sensor reproducibility is desired so that spatial transect data obtained by multiple sensors can be merged with minimal relative biases. Here we used the standard deviation of the offset between the Smart-T reading and the HOBO reference reading as a measure of reproducibility among the sensors. The standard deviation was 0.05°C for air temperature and 0.23% for RH.

The YNCenter experiment using I-Met sensors as references yielded similar standard deviations (0.03°C for air temperature and 0.18% for RH with I-Met 57232 as the reference; 0.04°C for air temperature and 0.33% for RH with I-Met 57540 as the reference). The offsets in RH were larger (median 9.14% in reference to I-Met 57232 and 5.80% in reference to I-Met 57540) than recorded in the YCEO experiment (median 3.40% in reference to HOBO).

b. Spatial variations in temperature and humidity

Figures 3 and 4 show the spatial variations of air temperature and RH measured with a Smart-T sensor (tag 6FD2) at 1400 and 2200 LT 24 and 31 July 2019 (visuals of some of the data in 3D are given in Figs. S3 and S4). The sensor clearly resolved the ranges of temperature (1.04°C at 2200 LT 24 July and 2.81°C at 1400 LT 31 July) and RH variations (up to 13% at 1400 LT 31 July) along the measurement route. The linear transect through an area with dense buildings in the west portion of the route generally showed higher temperatures than the more open route in the east. A persistent hot spot

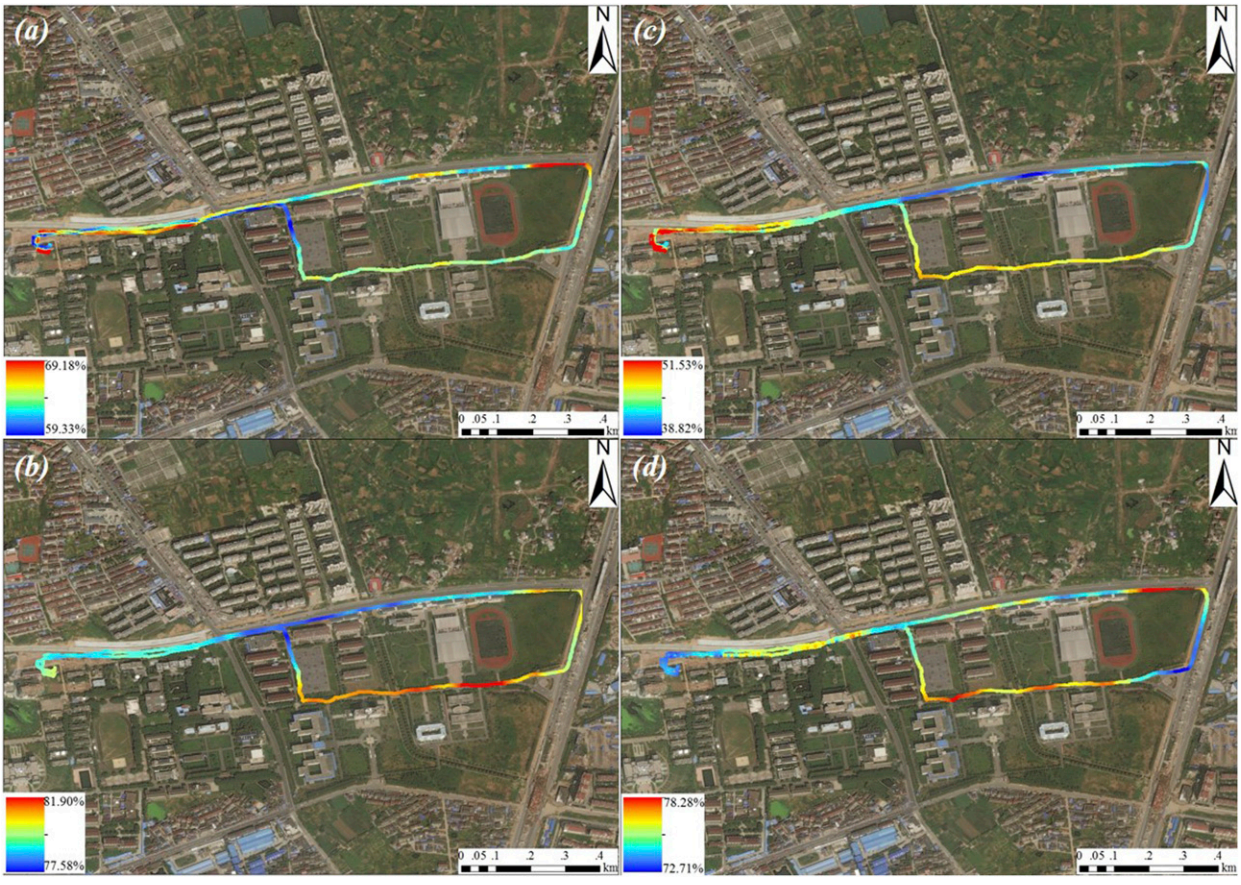

FIG. 4. As in Fig. 3, but for relative humidity.

occurred at the intersection between the linear transect and the loop. At 2200 LT 31 July (Fig. 3d), the highway was the warmest transect, having a temperature of 0.9°C above the whole-route mean of 30.04°C, possibly related to traffic heat emission at that time. No appreciable difference was observed between the two daytime and the two nighttime observations. The RH spatial variations appeared as mirror images of the temperature variations, showing lower values along the buildup transect and higher values in the more open transect. The results in Figs. 3 and 4, together with the data shown in Fig. 2, indicate that the Smart-T sensor can measure street-level air temperature and humidity with sufficient spatial resolutions and reasonable accuracy.

In Fig. 8, we show the relationship between temperature and vapor pressure anomaly, using all the data collected along the route shown in Figs. 3 and 4 and grouped according to time of the day. The anomaly is the difference between the actual value and the whole-route mean value during each observation. A positive and statistically significant relationship between air temperature and vapor pressure anomaly was found for the four times of the day (linear correlation r of 0.03–0.46, p value of 0–0.019, number of samples >6800). The highest correlation was observed in the early morning at 0500 LT ($r = 0.46$) and the lowest correlation at night (2200 LT, $r = 0.03$).

Examples of wet-bulb temperature T_w variations are given in Fig. 9. The spatial patterns were similar to those of air temperature (Fig. 3), indicating that air temperature exerted a dominant control over humidity on the T_w spatial variations. The range of wet-bulb temperature variations was 0.40°C (2200 LT 24 July; Fig. 3b) to 2.39°C (1400 LT 31 July; Fig. 3c), and was generally smaller than the range of dry bulb temperature variations, which was 1.04°C at 2200 LT 24 July (Fig. 3b) and 2.81°C at 1400 LT 31 July (Fig. 3c).

c. *Spatial correlations with land surface features*

Figures 10 and 11 show the spatial correlation of air temperature T_a, water vapor pressure or absolute humidity e_a and dewpoint temperature T_w with vegetation and impervious surface fractions in buffers of varying radius for two measurement times (1400 and 2200 LT). Here the buffer was a circular area drawn around each mobile measurement point. The correlation was first calculated for each of the seven observations along the transect shown in Fig. 3 and results in Figs. 10 and 11 represent the mean correlation value and the standard deviation of these observations. The T_a correlation was negative with vegetation fraction and positive with impervious surface fraction for both the daytime and the nighttime, over the range of buffer radius of 10 to 300 m. Over these buffer radii, the e_a correlation was also negative with vegetation fraction and positive with impervious surface fraction, although it was weaker than the T_a correlation.

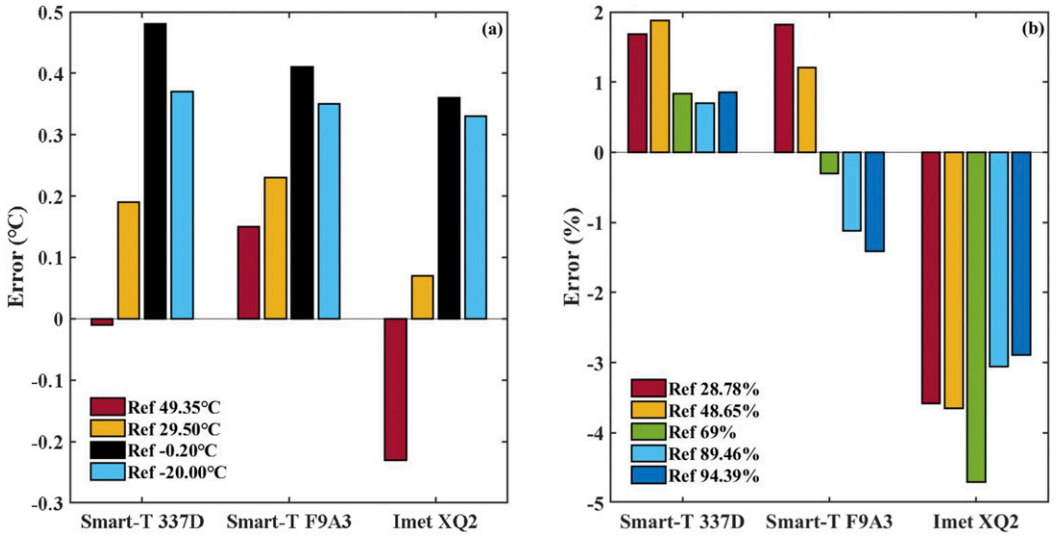

FIG. 5. (a) Characterization of errors in air temperature and (b) relative humidity measurements in the calibration chamber.

The source footprint size appeared different between the daytime and the nighttime and for T_a and e_a. In the daytime, the maximum correlation of T_a with vegetation fraction (-0.63) and impervious surface fraction ($+0.64$) occurred at a buffer radius of 10–30 m, and the correlation became gradually weaker with increasing radius. At the nighttime, the peak correlation, about -0.67 with vegetation fraction and $+0.67$ with impervious surface fraction, was found at a larger buffer radius of 50–80 m for vegetation fraction and 70–100 m for impervious surface fraction. These results indicate the air temperature source footprint was highly localized in the daytime and was slightly broader at night. The temperature footprint reported here was similar to that reported for Madison, Wisconsin (60–90 m, based on correlation with vegetation fraction; Ziter et al. 2019), and much smaller than that reported for Rotterdam, the Netherlands (about 700 m based on correlation with vegetation fraction and about 1600 m based on correlation with impervious surface fraction; Heusinkveld et al. 2014). No peak was identifiable for the e_a correlation with vegetation fraction or with the impervious surface fraction at either of the observation times. The e_a correlation with these two surface features showed a slight weakening trend with increasing buffer radius in the daytime. In the nighttime, the e_a correlation appeared invariant with radius.

The T_w correlations with vegetation fraction and impervious surface fractions were nearly identical to the T_a correlations, suggesting that air temperature dominated the T_w spatial variations and that the role of humidity was minor.

4. Discussion

a. *Comparison of accuracy with other mobile and distributed sensors*

Table S1 compares the accuracy of the Smart-T sensor with those found in the published urban studies involving mobile and spatially distributed sensors. The accuracy of the instruments in this literature survey lies in the range of $\pm 0.1°$ to $\pm 1°$C for temperature and $\pm 1.5\%$ to $\pm 5\%$ for RH. The Smart-T compares favorably with these instruments. Its RH accuracy (-1.4% to 1.9%) is about the same as that of the sensors recommended by WMO for operational weather monitoring (3%; WMO 2008), and its temperature accuracy in high temperature conditions ($-0.01°$ to 0.23°C; temperature >29°C) approaches the specifications for researcher-grade instruments (0.1°C; temperature in the range of $-40°$ to 40°C).

An important consideration in mobile observations is sensor time response. The Smart-T sensors have a time constant of 9.7 and 18.5 s for air temperature and RH, respectively. For comparison, the WMO guidelines recommend a response time of 20 s for temperature and 40 s for humidity (WMO 2008). The HOBO sensors used in the YNCenter indoor test and by Liu et al. (2017) for bicycle measurements have a temperature time constant of about 200 s (with radiation shield and moving at 1 m s^{-1}). The bicycle sensor used by Ziter et al. (2019) (model Campbell Scientific 109SS; Table S1) has a temperature time constant of 7.5 s (without radiation shield and moving at 3 m s^{-1}). The wireless temperature sensor described by Young et al. (2014) has a time constant of 110 s. Ideally, the sensor time response should match its speed of motion. If vehicles are the measurement platform, fast-responding sensors, such as fine-wire thermocouples (Makido et al. 2016; Voelkel and Shandas 2017; Shandas et al. 2019), are preferred over standard (slow) sensors to produce adequate spatial variations. A standard sensor with time response of 20–40 s on a vehicle moving at a speed of 30 km h^{-1} cannot resolve variations at spatial scales smaller than 167–330 m. On the other hand, too short a time constant is not desirable on a slow platform because random turbulent fluctuations recorded by the sensor will confound data interpretation. In this context, the Smart-T time responses appear appropriate for deployment on bicycles (e.g., Fig. 2).

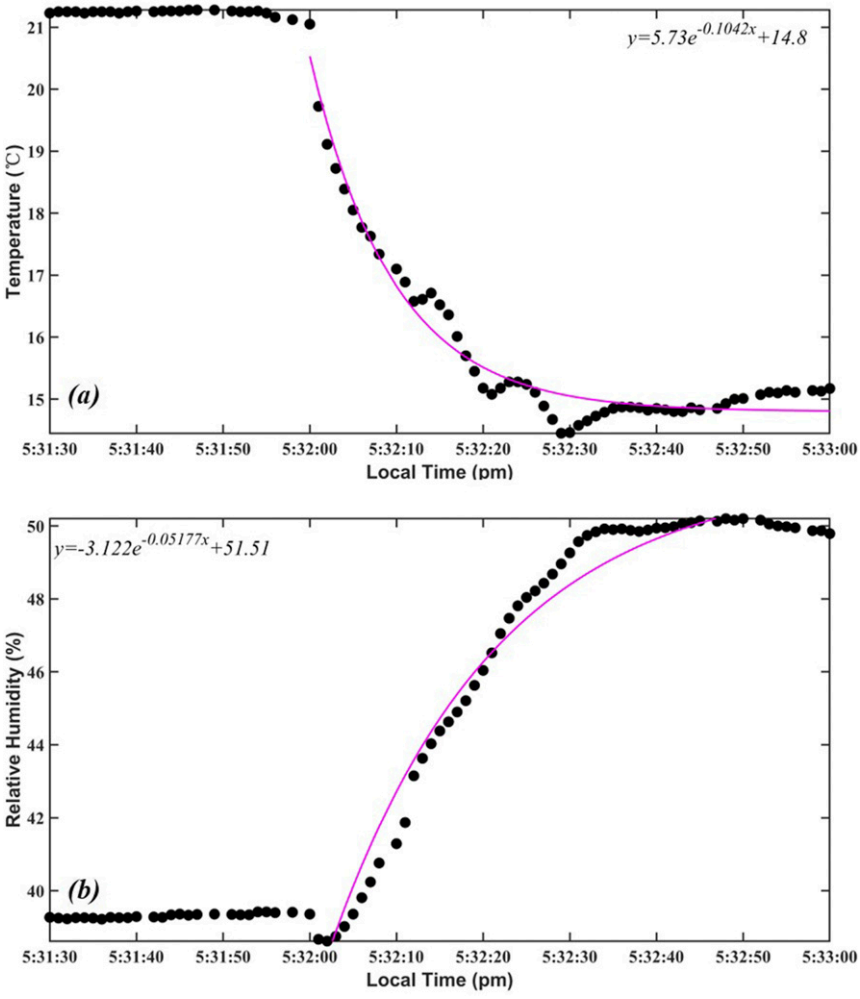

FIG. 6. Smart-T measurement in response to a step change in (a) air temperature and (b) relative humidity. The smooth curves are regression fitting. The independent variable x in the regression equation is time elapsed (s) since 1732:00 LT (time is formatted as H:MM:SS on the x axes).

b. IoT and sensor reproducibility

The Smart-T sensors have several key features of the IoT technology. At a fraction of the cost [<$100 (U.S. dollars) per complete unit, roughly 80% of which is the cost of making the radiation shelter] of instruments used for weather stations, they can be deployed in large quantities. They take full advantage of Bluetooth and GPS functions already embedded in smartphones, enabling connectivity and geolocation. No special training is required to operate these sensors, so volunteer cyclists and citizen scientists can easily take part in data collection.

Crowdsourcing or citizen science has the potential to expand the spatial and temporal data coverage beyond the limits of traditional stationary monitoring. Data quality is a key factor that determines the utility of crowdsourcing data (Castell et al. 2015; Meier et al. 2017). Only through rigorous quality controls can useful conclusions be drawn from crowdsourced data. This challenge poses a high requirement for sensor reproducibility and accuracy. In mobile observations that aim to quantify temporal and spatial variations, reproducibility among multiple sensors is more important than absolute accuracy. The Smart-T reproducibility, measured as one standard deviation of the offset from a reference, was 0.03°–0.05°C for temperature and 0.18%–0.33% for RH (Fig. 7). The actual reproducibility should be better than these because these standard deviations were affected by the measurement noise of the reference sensor. The performance reported here is better than the reproducibility of the temperature sensors (0.12°C) used in a crowdsourcing experiment (Meier et al. 2017; one standard deviation of the data in their Fig. 2a).

Further improvement to Smart-T data quality may be made by accounting for the offset of each individual sensor, as long as the batch of sensors deployed in the study is calibrated against the same working reference standard. A lookup table of offset values and the associated Bluetooth tags, prepared prior to field deployment and based on a calibration test, can be used for postfield correction of the data. For example, the Smart-T sensor (tag 6FD2) used in the transect experiment shown

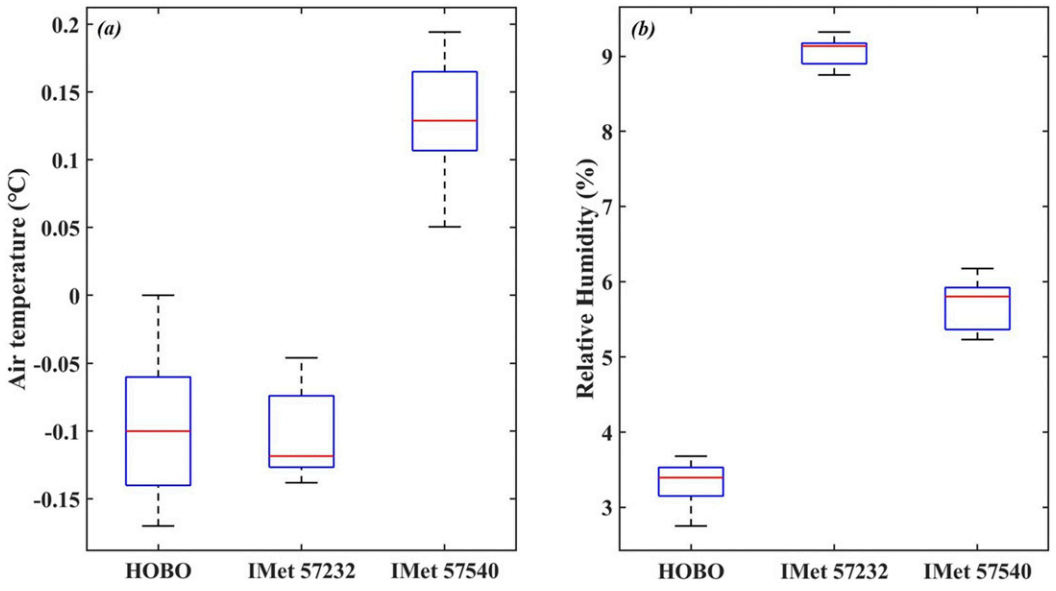

FIG. 7. A box-and-whisker plot showing the offset of (a) air temperature and (b) relative humidity between Smart-T sensors and three reference sensors (HOBO, I-Met XQ2 57232, and I-Met XQ2 57540) in the two indoor tests. The horizontal red line marks the median value, the box represents the middle 50th percentile, and the top and the bottom ends of the whiskers mark the maximum and the minimum value, respectively. Offset is calculated as the Smart-T reading minus the reference reading.

in Fig. 2 had an offset of 0.11°C for temperature and 5.89% for RH against the reference sensor (I-Met 57540). The same reference sensor was also used in the transect intercomparison experiment. After removing these offsets from the transect data, the temperature discrepancy between the two sensors was reduced slightly from 0.07° to −0.05°C, although the humidity discrepancy did not improve (from 2.6% to −3.0%).

According to Meier et al. (2017) and Venter et al. (2020), two other sources of error, radiation interference and erroneous

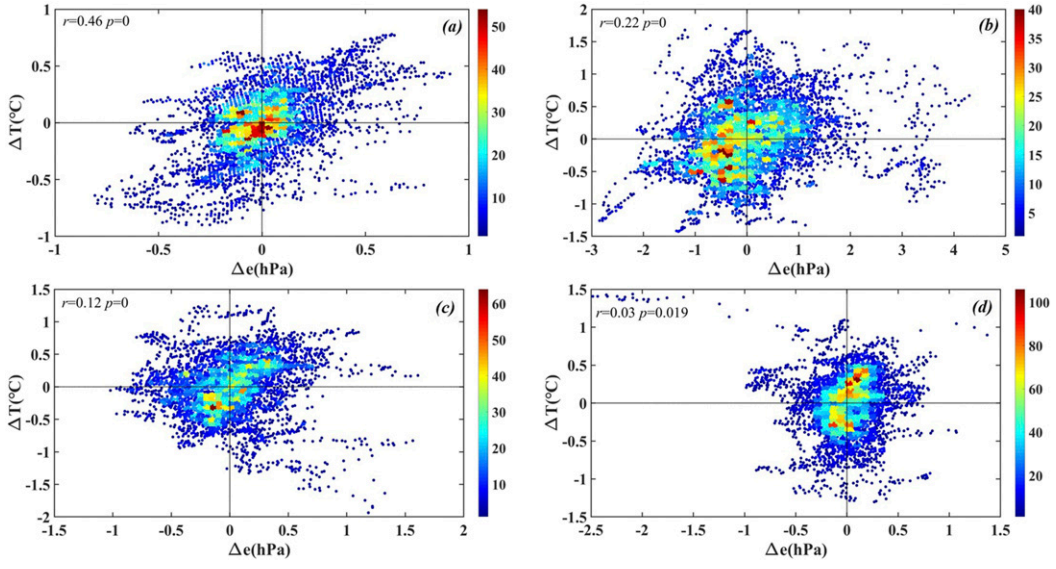

FIG. 8. Relationship between vapor pressure anomaly and air temperature anomaly at (a) 0500, (b) 1400, (c) 1900 and (d) 2200 LT using all observations along the route shown in Fig. 3. The color scale shows data density. Anomaly is the difference between the actual value and the whole-route mean value for each observation. Also shown are the linear correlation coefficient (r) and the statistical significance (p).

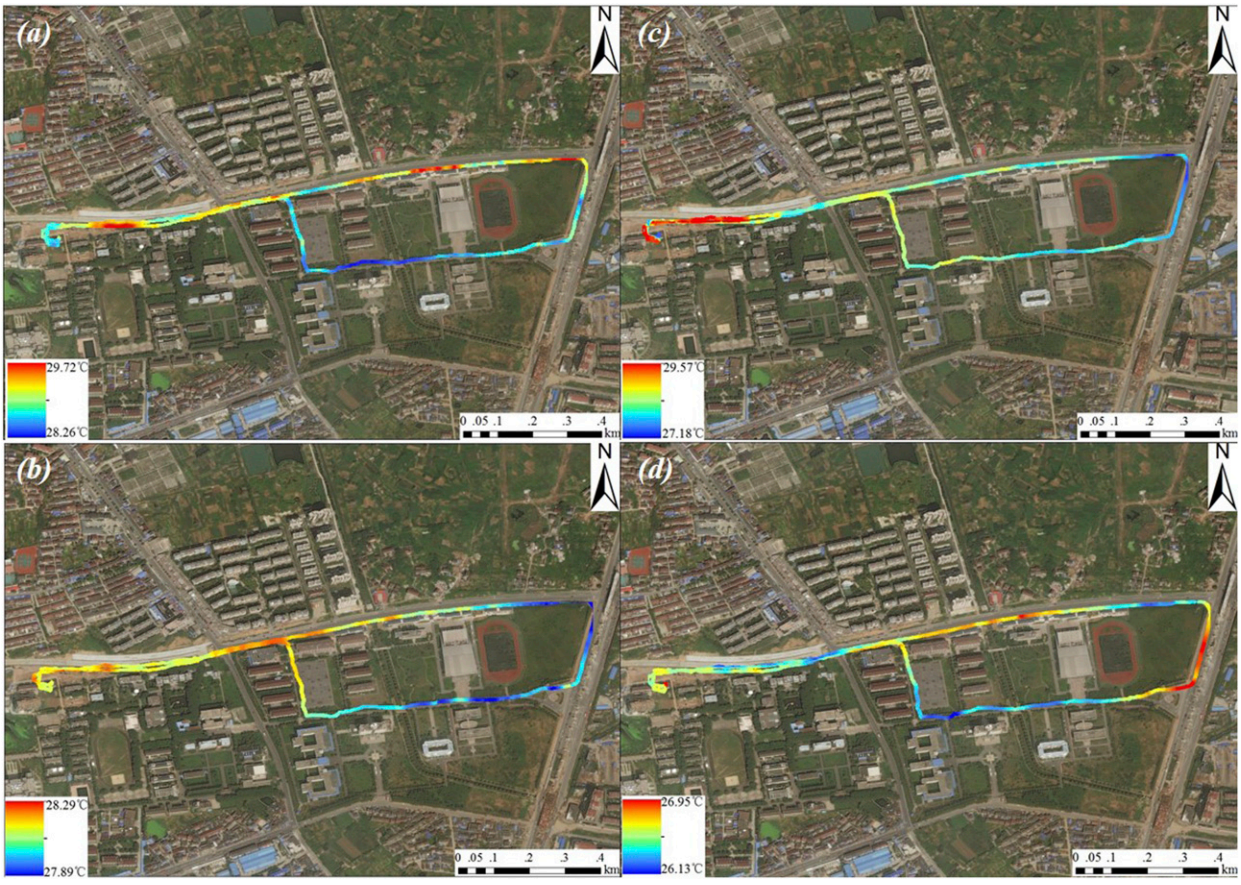

FIG. 9. Spatial variations in wet-bulb temperature at (a) 1400 and (b) 2200 LT 24 Jul and (c) 1400 and (d) 2200 LT 31 Jul 2019. The map background is a true-color satellite image.

meta information on sensor position, can degrade the quality of the temperature data collected with distributed IoT sensors. We have not done a rigorous evaluation of the Smart-T radiation shelter housing (Fig. 1a). As shown in Fig. 2, excellent agreement between the Smart-T and the I-Met sensor (0.05°C) was found during an outdoor test under bright sunlight (solar radiation: 317 $W\,m^{-2}$), suggesting that radiation contamination was minimal, at least when the bicycle was moving at a normal speed. In this experiment, radiation interference on the I-Met unit should be negligible because its sensor was very small (6 mm in diameter) and it was placed under a homemade white radiation shelter with ventilation. Regarding sensor positioning, because coordinate information is updated for each data sample, data collected inadvertently, such as when the sensor is still indoors or when the bicycle is in a parked position, can be easily identified and removed.

The Smart-T sensor relies on bicycle motion to promote ventilation and to reduce radiation error. Whether its radiation shield offers adequate ventilation via natural air motion has not been evaluated. A larger shield (e.g., Young et al. 2014) may be required for stationary monitoring (but without the need to change other components of the sensor).

c. Relationship between temperature, humidity, and surface morphology

Our street transect data showed that air temperature and absolute humidity variations were positively correlated (Fig. 8). This correlation pattern arose from their covariations with urban surface features. According to Figs. 10 and 11, increasing vegetation fraction was associated with both temperature and absolute humidity reductions, and increasing impervious surface fraction had the opposite effect. One inference from these results is that expanding urban vegetation could relief heat stress on both fronts, by lowering air temperature and humidity.

The intracity spatial correlation between temperature and absolute humidity in the present study differed from two other urban mobile studies found in the literature. The mobile measurement made in street transects of Gaborone, Botswana (Jonsson 2004), revealed a negative correlation between these two variables at night (spatial correlation = −0.47, $p < 0.01$, based on the data presented in their Figs. 9 and 10). The second mobile study, carried out in Padua, Italy (Noro et al. 2015), only presented one evening transect and the results revealed a weak negative correlation (spatial correlation = −0.28, $p = 0.33$, based on the data presented in their Figs. 7 and 8). One reason for this difference may be related to the background

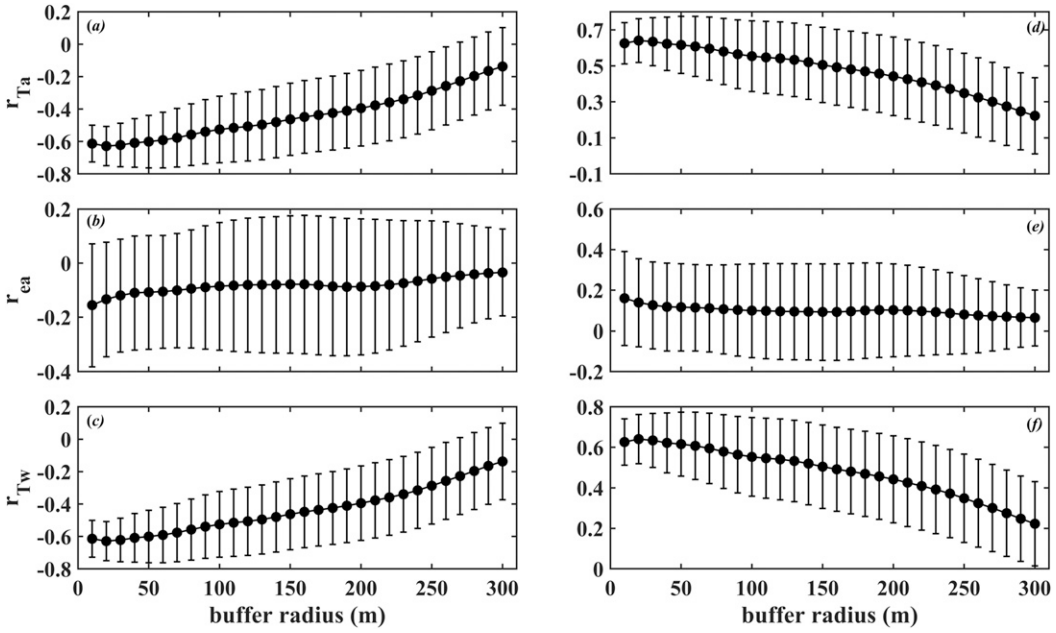

FIG. 10. Spatial correlation of air temperature (T_a), water vapor pressure (e) and wet-bulb temperature (T_w) as functions of buffer radius at 1400 LT. (a)–(c) Correlations with vegetation fraction and (d)–(f) correlations with impervious surface fraction. Error bars are ±1 standard deviation of seven observations.

climatic influence. The City of Nanjing is influenced by the Asian monsoon, with abundant precipitation in the summer, whereas Gaborone is located in a semiarid climate zone.

It is instructive to compare the intracity spatial correlation with temporal correlation from urban–rural site pair analysis. According to the observations in London, United Kingdom (Lee 1991), Goteborg, Sweden (Holmer and Eliasson 1999), Munich, Germany (Mayer et al. 2003), and Krefeld, Germany (Kuttler et al. 2007), the urban air is generally more moist than the rural air at night, and the urban–rural differences in absolute humidity and in air temperature are positively correlated over time. In other words, at times when the UHI is stronger, the urban moisture excess is also greater. Several mechanisms are proposed by these studies to explain this

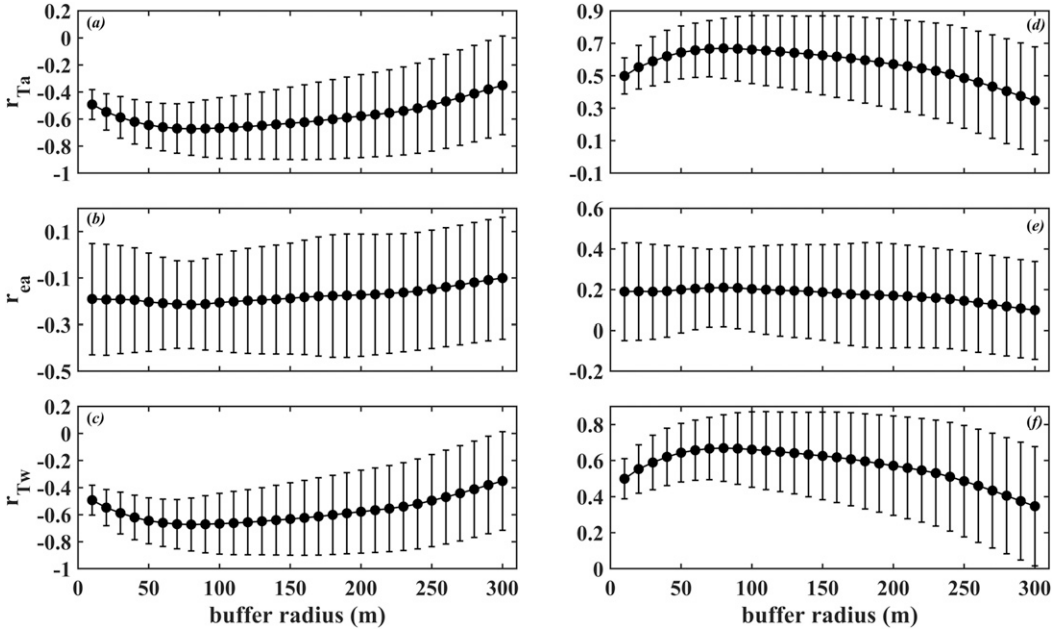

FIG. 11. As in Fig. 10, but at 2200 LT.

temporal correlation, including water vapor emission by automobile engines, removal of water vapor from rural air by dew formation, and longwave radiation feedback on the UHI associated with the urban moisture excess. These mechanisms operate at the whole-city scale. At the neighborhood scale and the scale of landscape patches, the interplay between temperature, humidity and surface morphology may reflect local moisture limitation and energy availability. It appears that the landscape in Nanjing was more limited by energy than by soil moisture. We suggest that locations with lower fraction of vegetation and higher fraction of impervious surface generally had higher absorption of solar radiation and higher amount of anthropogenic heat release, and a greater level of available energy, in turn, would lead to higher air temperature and higher humidity through enhanced sensible and latent heat flux.

5. Conclusions

The Smart-T sensor achieved accuracy and reproducibility nearly comparable to those of research-grade sensors. Its time response was adequate for capturing neighborhood-scale spatial variations (40–70 m). Because it simultaneously measure air temperature and air humidity, it should give a better measure of human thermal comfort than sensors that measure only air temperature. No training is required to operate the sensor, so it is possible to expand the measurement with the help of volunteer cyclists and citizen scientists.

Street transect data in Nanjing showed that increasing vegetation fraction caused reduction in both air temperature and absolute humidity and that increasing impervious surface fraction had the opposite effect, in both daytime and nighttime. Because of their covariations with vegetation and impervious cover, air temperature and absolute humidity were positively correlated in space. The maximum correlation of temperature with these surface morphological parameters occurred at a buffer radius of 10–30 m in the daytime and 50–100 m at night, indicating that the temperature source footprint was highly localized. In comparison, no correlation peak was discernible for absolute humidity, suggesting that the humidity spatial variations were associated with larger-scale processes than temperature variations.

Acknowledgments. This work was supported by the National Key R&D Program of China (Grant 2019YFA0607202 to CC), the Leitner Award for Uncommon Collaboration (to XL), the Natural Science Foundation of Jiangsu Province (Grants BK20180796 BK20181100 to CC and JX, respectively), and the National Natural Science Foundation of China (Grant 41805022 to JX). The first author acknowledges the support from the Startup Foundation for Introducing Talent of NUIST (Grant 2017r067).

REFERENCES

Arnfield, A. J., 2003: Two decades of urban climate research: A review of turbulence, exchanges of energy and water, and the urban heat island. *Int. J. Climatol.*, **23**, 1–26, https://doi.org/10.1002/joc.859.

Basara, J. B., and Coauthors, 2011: The Oklahoma City Micronet. *Meteor. Appl.*, **18**, 252–261, https://doi.org/10.1002/MET.189.

Bowler, D. E., L. Buyung-Ali, T. M. Knight, and A. S. Pullin, 2010: Urban greening to cool towns and cities: A systematic review of the empirical evidence. *Landscape Urban Plann.*, **97**, 147–155, https://doi.org/10.1016/j.landurbplan.2010.05.006.

Brandsma, T., and D. Wolters, 2012: Measurement and statistical modeling of the urban heat island of the city of Utrecht (The Netherlands). *J. Appl. Meteor. Climatol.*, **51**, 1046–1060, https://doi.org/10.1175/JAMC-D-11-0206.1.

Castell, N., M. Kobernus, H. Y. Liu, P. Schneider, W. Lahoz, A. Berre, and J. Noll, 2015: Mobile technologies and services for environmental monitoring: The Citi-Sense-MOB approach. *Urban Climate*, **14**, 370–382, https://doi.org/10.1016/j.uclim.2014.08.002.

Chakraborty, T., A. Hsu, D. Manya, and G. Sheriff, 2019: Disproportionately higher exposure to urban heat in lower-income neighborhoods: A multi-city perspective. *Environ. Res. Lett.*, **14**, 105003, https://doi.org/10.1088/1748-9326/ab3b99.

Chapman, L., C. L. Muller, D. T. Young, E. L. Warren, C. S. B. Grimmond, X. M. Cai, and E. J. S. Ferranti, 2015: The Birmingham Urban Climate Laboratory: An open meteorological test bed and challenges of the smart city. *Bull. Amer. Meteor. Soc.*, **96**, 1545–1560, https://doi.org/10.1175/BAMS-D-13-00193.1.

Chen, Y., C. Yao, T. Honjo, and T. Lin, 2018: The application of a high-density street-level air temperature observation network (HiSAN): Dynamic variation characteristics of urban heat island in Tainan, Taiwan. *Sci. Total Environ.*, **626**, 555–566, https://doi.org/10.1016/j.scitotenv.2018.01.059.

Chhetri, D. B., Y. Fujimori, and R. Moriwaki, 2017: Local climate classification and urban heat/dry island in Matsuyama plain. *J. Japan Soc. Civil Eng.*, **73B1**, 487–492, https://doi.org/10.2208/JSCEJHE.73.I_487.

Cohen, P., O. Potchter, and A. Matzarakis, 2012: Daily and seasonal climatic conditions of green urban open spaces in the Mediterranean climate and their impact on human comfort. *Build. Environ.*, **51**, 285–295, https://doi.org/10.1016/j.buildenv.2011.11.020.

Droste, A. M., J. J. Pape, A. Overeem, H. Leijnse, G. J. Steeneveld, A. J. Delden, and R. Uijlenhoet, 2017: Crowdsourcing urban air temperatures through smartphone battery temperatures in São Paulo, Brazil. *J. Atmos. Oceanic Technol.*, **34**, 1853–1866, https://doi.org/10.1175/JTECH-D-16-0150.1.

Gong, P., and Coauthors, 2020: Annual maps of global artificial impervious area (GAIA) between 1985 and 2018. *Remote Sens. Environ.*, **236**, 111510, https://doi.org/10.1016/j.rse.2019.111510.

Grimmond, C. S. B., 2006: Progress in measuring and observing the urban atmosphere. *Theor. Appl. Climatol.*, **84**, 3–22, https://doi.org/10.1007/s00704-005-0140-5.

Gunawardena, K. R., M. J. Wells, and T. Kershaw, 2017: Utilising green and bluespace to mitigate urban heat island intensity. *Sci. Total Environ.*, **584–585**, 1040–1055, https://doi.org/10.1016/j.scitotenv.2017.01.158.

Hammerberg, K., O. Brousse, A. Martilli, and A. Mahdavi, 2018: Implications of employing detailed urban canopy parameters for mesoscale climate modelling: A comparison between WUDAPT and GIS databases over Vienna, Austria. *Int. J. Climatol.*, **38**, e1241–e1257, https://doi.org/10.1002/joc.5447.

Hedquist, B. C., and A. J. Brazel, 2006: Urban, residential, and rural climate comparisons from mobile transects and fixed stations: Phoenix, Arizona. *J. Ariz.-Nev. Acad. Sci.*, **38**, 77–87, https://doi.org/10.2181/1533-6085(2006)38[77:URARCC]2.0.CO;2.

Heusinkveld, B. G., G. J. Steeneveld, L. W. A. van Hove, C. M. J. Jacobs, and A. A. M. Holtslag, 2014: Spatial variability of the Rotterdam urban heat island as influenced by urban land use. *J. Geophys. Res. Atmos.*, **119**, 677–692, https://doi.org/10.1002/2012JD019399.

Ho, H. C., A. Knudby, P. Sirovyak, Y. Xu, M. Hodul, and S. B. Henderson, 2014: Mapping maximum urban air temperature on hot summer days. *Remote Sens. Environ.*, **154**, 38–45, https://doi.org/10.1016/j.rse.2014.08.012.

Holmer, B., and I. Eliasson, 1999: Urban–rural vapor pressure differences and their role in the development of urban heat islands. *Int. J. Climatol.*, **19**, 989–1009, https://doi.org/10.1002/(SICI)1097-0088(199907)19:9<989::AID-JOC410>3.0.CO;2-1.

Horst, T. W., 2001: Comments on "Footprint analysis: A closed analytical solution based on height-dependent profiles of wind speed and eddy viscosity." *Bound.-Layer Meteor.*, **101**, 435–447, https://doi.org/10.1023/A:1019250918341.

Hung, T. K., and O. C. Wo, 2012: Development of a community weather information network in Hong Kong. *Weather*, **67**, 48–50, https://doi.org/10.1002/wea.1883.

Jiang, S., X. Lee, J. Wang, and K. Wang, 2019: Amplified urban heat islands during heat wave periods. *J. Geophys. Res. Atmos.*, **124**, 7797–7812, https://doi.org/10.1029/2018JD030230.

Jonsson, P., 2004: Vegetation as an urban climate control in the subtropical city of Gaborone, Botswana. *Int. J. Climatol.*, **24**, 1307–1322, https://doi.org/10.1002/joc.1064.

Koskinen, J. T., and Coauthors, 2011: The Helsinki Testbed: A mesoscale measurement, research, and service platform. *Bull. Amer. Meteor. Soc.*, **92**, 325–342, https://doi.org/10.1175/2010BAMS2878.1.

Kuttler, W., S. Weber, J. Schonnefeld, and A. Hesselschwerdt, 2007: Urban/rural atmospheric water vapor pressure differences and urban moisture excess in Krefeld, Germany. *Int. J. Climatol.*, **27**, 2005–2015, https://doi.org/10.1002/joc.1558.

Leconte, F., J. Bouyer, R. Claverie, and M. Pétrissans, 2017: Analysis of nocturnal air temperature in districts using mobile measurements and a cooling indicator. *Theor. Appl. Climatol.*, **130**, 365–376, https://doi.org/10.1007/s00704-016-1886-7.

Lee, D. O., 1991: Urban–rural humidity differences in London. *Int. J. Climatol.*, **11**, 577–582, https://doi.org/10.1002/joc.3370110509.

Lee, X., 2018: *Fundamentals of Boundary-Layer Meteorology*. Springer International Publishing, 195 pp.

Li, H., F. Meier, X. Lee, T. Chakraborty, J. Liu, M. Schaap, and S. Sodoudi, 2018: Interaction between urban heat island and urban pollution island during summer in Berlin. *Sci. Total Environ.*, **636**, 818–828, https://doi.org/10.1016/j.scitotenv.2018.04.254.

Li, X., Y. Zhou, Z. Zhu, and W. Cao, 2020: A national dataset of 30 m annual urban extent dynamics (1985-2015) in the conterminous United States. *Earth Syst. Sci. Data*, **12**, 357–371, https://doi.org/10.5194/essd-12-357-2020.

Liu, L., Y. Lin, J. Liu, D. Wang, T. Shui, X. Chen, and Q. Wu, 2017: Analysis of local-scale urban heat island characteristics using an integrated method of mobile measurement and GIS-based spatial interpolation. *Build. Environ.*, **117**, 191–207, https://doi.org/10.1016/j.buildenv.2017.03.013.

Makido, Y., V. Shandas, S. Ferwati, and D. Sailor, 2016: Daytime variation of urban heat islands: The case study of Doha, Qatar. *Climate*, **4**, 32, https://doi.org/10.3390/cli4020032.

Mayer, H., A. Matzarakis, and M. G. Iziomon, 2003: Spatio-temporal variability of moisture conditions within the urban canopy layer. *Theor. Appl. Climatol.*, **76**, 165–179, https://doi.org/10.1007/s00704-003-0010-y.

Meier, F., D. Fenner, T. Grassmann, M. Otto, and D. Scherer, 2017: Crowdsourcing air temperature from citizen weather stations for urban climate research. *Urban Climate*, **19**, 170–191, https://doi.org/10.1016/j.uclim.2017.01.006.

Mirzaei, P. A., and F. Haghighat, 2010: Approaches to study urban heat island—Abilities and limitations. *Build. Environ.*, **45**, 2192–2201, https://doi.org/10.1016/j.buildenv.2010.04.001.

Moratiel, R., B. Soriano, A. Centeno, D. Spano, and R. L. Snyder, 2017: Wet-bulb, dew point, and air temperature trends in Spain. *Theor. Appl. Climatol.*, **130**, 419–434, https://doi.org/10.1007/s00704-016-1891-x.

Muller, C. L., L. Chapman, C. S. B. Grimmond, D. T. Young, and X. Cai, 2013: Sensors and the city: A review of urban meteorological networks. *Int. J. Climatol.*, **33**, 1585–1600, https://doi.org/10.1002/joc.3678.

——, ——, S. Johnson, C. Kidd, S. Illingworth, G. Foody, A. Overeem, and R. R. Leigh, 2015: Crowdsourcing for climate and atmospheric sciences: Current status and future potential. *Int. J. Climatol.*, **35**, 3185–3203, https://doi.org/10.1002/joc.4210.

Noro, M., F. Busato, and R. M. Lazzarin, 2015: Urban heat island in Padua, Italy: Experimental and theoretical analysis. *Indoor Built Environ.*, **24**, 514–533, https://doi.org/10.1177/1420326X13517404.

Oke, T. R., 2006: Initial guidance to obtain representative meteorological observations at urban sites. WMO Rep. 81, 51 pp.

——, G. Mills, A. Christen, and J. A. Voogt, 2017: *Urban Climates*. Cambridge University Press, 519 pp.

Overeem, A., J. C. R. Robinson, H. Leijnse, G. J. Steeneveld, B. K. P. Horn, and R. Uijlenhoet, 2013: Crowdsourcing urban air temperatures from smartphone battery temperatures. *Geophys. Res. Lett.*, **40**, 4081–4085, https://doi.org/10.1002/grl.50786.

Pigliautile, I., and A. L. Pisello, 2018: A new wearable monitoring system for investigating pedestrians' environmental conditions: Development of the experimental tool and start-up findings. *Sci. Total Environ.*, **630**, 690–706, https://doi.org/10.1016/j.scitotenv.2018.02.208.

Qaid, A., H. B. Lamit, D. R. Ossen, and R. N. R. Shahminan, 2016: Urban heat island and thermal comfort conditions at microclimate scale in a tropical planned city. *Energy Build.*, **133**, 577–595, https://doi.org/10.1016/j.enbuild.2016.10.006.

Rajkovich, N. B., and L. Larsen, 2016: A bicycle-based field measurement systems for the study of thermal exposure in Cuyahoga County, Ohio, USA. *Int. J. Environ. Res. Public Health*, **13**, 159, https://doi.org/10.3390/ijerph13020159.

Revi, A., D. E. Satterthwaite, F. Aragón-Durand, J. Corfee-Morlot, R. B. R. Kiunsi, M. Pelling, D. C. Roberts, and W. Solecki, 2014: Urban areas. *Climate Change 2014: Impacts, Adaptation, and Vulnerability*, C. B. Field et al., Eds., Cambridge University Press, 535–612.

Runkle, J. D., C. Cui, C. Fuhrmann, S. Stevens, J. D. Pinal, and M. M. Sugg, 2019: Evaluation of wearable sensors for physiologic monitoring of individually experienced temperatures in outdoor workers in southeastern U.S. *Environ. Int.*, **129**, 229–238, https://doi.org/10.1016/j.envint.2019.05.026.

Schatz, J., and C. J. Kucharik, 2014: Seasonality of the urban island effect in Madison, Wisconsin. *J. Appl. Meteor. Climatol.*, **53**, 2371–2386, https://doi.org/10.1175/JAMC-D-14-0107.1.

Schmid, H. P., 2002: Footprint modeling for vegetation atmosphere exchange studies: A review and perspective. *Agric. For. Entomol.*, **113**, 159–183, https://doi.org/10.1016/s0168-1923(02)00107-7.

Scott, A., and Coauthors, 2017: Temperature and heat in informal settlements in Nairobi. *PLOS ONE*, **12**, e0187300, https://doi.org/10.1371/JOURNAL.PONE.0187300.

Shandas, V., J. Voelkel, J. Williams, and J. Hoffman, 2019: Integrating satellite and ground measurements for predicting locations of extreme urban heat. *Climate*, **7**, 5, https://doi.org/10.3390/cli7010005.

Sherwood, S. C., and M. Huber, 2010: An adaptability limit to climate change due to heat stress. *Proc. Natl. Acad. Sci. USA*, **107**, 9552–9555, https://doi.org/10.1073/pnas.0913352107.

Shi, Y., K. K. Lau, C. Ren, and E. Ng, 2018: Evaluating the local climate zone classification in high-density heterogeneous urban environment using mobile measurement. *Urban Climate*, **25**, 167–186, https://doi.org/10.1016/j.uclim.2018.07.001.

Tsin, P. K., A. Knudby, E. S. Krayenhoff, H. C. Ho, M. Brauer, and S. B. Henderson, 2016: Microscale mobile monitoring of urban air temperature. *Urban Climate*, **18**, 58–72, https://doi.org/10.1016/j.uclim.2016.10.001.

Unger, J., Z. Sümeghy, and J. Zoboki, 2001: Temperature cross-section features in an urban area. *Atmos. Res.*, **58**, 117–127, https://doi.org/10.1016/S0169-8095(01)00087-4.

Venter, Z., O. Brousse, I. Esau, and F. Meier, 2020: Hyperlocal mapping of urban air temperature using remote sensing and crowdsourced weather data. *Remote Sens. Environ.*, **242**, 111791, https://doi.org/10.1016/j.rse.2020.111791.

Voelkel, J., and V. Shandas, 2017: Towards systematic prediction of urban heat islands: Grounding measurements, assessing modeling techniques. *Climate*, **5**, 41, https://doi.org/10.3390/cli5020041.

Voogt, J. A., and T. R. Oke, 2003: Thermal remote sensing of urban climates. *Remote Sens. Environ.*, **86**, 370–384, https://doi.org/10.1016/S0034-4257(03)00079-8.

Wang, K., S. Jiang, J. Wang, C. Zhou, X. Wang, and X. Lee, 2018: Comparing the diurnal and seasonal variabilities of atmospheric and surface urban heat islands based on the Beijing urban meteorological network. *J. Geophys. Res. Atmos.*, **122**, 2131–2154, https://doi.org/10.1002/2016JD025304.

Warren, E. L., D. T. Young, L. Chapman, C. Muller, C. S. B. Grimmond, and X. M. Cai, 2016: The Birmingham Urban Climate Laboratory—A high density, urban meteorological dataset, from 2012-2014. *Sci. Data*, **3**, 160038, https://doi.org/10.1038/sdata.2016.38.

WMO, 2008: Guide to meteorological instruments and methods of observation. 7th ed. WMO Rep. 8, 716 pp., http://library.wmo.int/pmb_ged/wmo_8_en-2012.pdf.

Yan, H., S. Fan, C. Guo, F. Wu, N. Zhang, and L. Dong, 2014: Assessing the effects of landscape design parameters on intra-urban air temperature variability: The case of Beijing, China. *Build. Environ.*, **76**, 44–53, https://doi.org/10.1016/j.buildenv.2014.03.007.

——, F. Wu, and L. Dong, 2018: Influence of a large urban park on the local urban thermal environment. *Sci. Total Environ.*, **622–623**, 882–891, https://doi.org/10.1016/j.scitotenv.2017.11.327.

Yang, J., and E. Bou-Zeid, 2019: Designing sensor networks to resolve spatio-temporal urban temperature variations: Fixed, mobile or hybrid? *Environ. Res. Lett.*, **14**, 074022, https://doi.org/10.1088/1748-9326/ab25f8.

Yokoyama, H., R. Ooka, and H. Kikumoto, 2018: Study of mobile measurements for detailed temperature distribution in a high-density urban area in Tokyo. *Urban Climate*, **24**, 517–528, https://doi.org/10.1016/j.uclim.2017.06.006.

Young, D. T., L. Chapman, C. L. Muller, and X. Cai, 2014: A low-cost wireless temperature sensor: Evaluation for use in environmental monitoring applications. *J. Atmos. Oceanic Technol.*, **31**, 938–944, https://doi.org/10.1175/JTECH-D-13-00217.1.

Zhao, L., X. Lee, and N. Schultz, 2017: A wedge strategy for mitigation of urban warming in future climate scenarios. *Atmos. Chem. Phys.*, **17**, 9067–9080, https://doi.org/10.5194/acp-17-9067-2017.

Zhou, D., and Coauthors, 2019: Satellite remote sensing of surface urban heat islands: Progress, challenges, and perspectives. *Remote Sens.*, **11**, 48, https://doi.org/10.3390/rs11010048.

Ziter, C. D., E. J. Pedersen, C. J. Kucharik, and M. G. Turner, 2019: Scale-dependent interactions between tree canopy cover and impervious surface reduce daytime urban heat during summer. *Proc. Natl. Acad. Sci. USA*, **116**, 7575–7580, https://doi.org/10.1073/pnas.1817561116.